Communication

The Fatal Defects in Cast Al-Si Alloys Due to Sn Addition

Yao Xiao , Jicheng Wang , Qianyu Deng , Li Feng , Dianming Peng , Hui Feng , Kai Li * , Yong Du

Posted Date: 14 July 2023

doi: 10.20944/preprints202307.0963.v1

Keywords: Al-Si alloys; cast defect; Sn; Sn oxides; FIB; HADDF-STEM

Communication

The Fatal Defects in Cast Al-Si Alloys Due to Sn Addition

Yao Xiao [1], Jicheng Wang [3] Qianyu Deng [3], Li Feng [3], Dianming Peng [3], Hui Feng [4], Kai Li [1,2,*] and Yong Du [1,2]

[1] State Key Laboratory of Powder Metallurgy, Central South University, Changsha 410083, China; yong-du@csu.edu.cn
[2] Hunan Center for Electron Microscopy, Central South University, Changsha 410083, China; leking@csu.edu.cn
[3] Runxingtai Electric Appliance Co., Ltd., Zhuhai 519000, China; jichengwang@yc-dc.com
[4] Research Institute for Aerospace Manufacturing Technology, Nanjing Chenguang Group Co., Ltd., Nanjing 210006, China; fenghuihui22@126.com
* Correspondence: leking@csu.edu.cn; Tel.: +86-18973163497

Abstract: The cast defects strongly degrade the mechanical properties in cast alloys. The effect of Sn addition on Al-Si alloys was investigated by 3D computed tomography, SEM and TEM. Amorphous Sn oxides are found near the alumina film, cause more shrinkage pores, initiate cracks and deteriorate mechanical properties. This work suggests not adding Sn in various Al alloys used in cast state.

Keywords: Al-Si alloys; cast defect; Sn; Sn oxides; FIB; HADDF-STEM

1. Introduction

The unibody casting technology of car manufacturing initiated a major revolution in the die-cast aluminum alloy industry [1]. To minimize cost, heat treatments are cancelled in this technology. Among all aluminum alloys, Al-Si alloys with outstanding castability are most suitable for such a technology. Cast defects, like shrinkage, pores and oxides, are common in Al-Si alloys and strongly degrade the mechanical properties [2]. However, unlike wrought Al alloys such as the 6000 and 7000 series, cast defects of Al-Si alloys cannot be reduced by deformation processes. Therefore, it's very important to strictly control cast defects.

Besides the parameters of casting [3], compositions also strongly affect cast defects in Al-Si alloys. The plate-like β-AlFeSi always generates in Al-Si alloys with Fe addition, which increased the porosity during solidification by blocking liquids feeding channels [4,5]. Mn addition can transform β-AlFeSi phases to Chinese script like α-AlFeMnSi phases [5,6], contributing to the reduction of porosity.

In recent years, the strengthening effects of Sn have been found in various wrought and cast Al alloys [7–14]. The mechanism has been revealed by the work of Elsayed et al. [15] on a model Al-0.025 at.% Sn cast alloy. They found that Sn solutes effectively trap and release the vacancies during quenching and heat treatments, respectively. Thus, when Sn was added to age hardenable alloys such as Al-Cu, the θ′ precipitates were likely to finely distribute in a high number density in subsequent heat treatments. Similarly, in the cast Al-7 wt.% Si-7 wt.% Cu alloy studied by Akopyan [13] et al., the addition of 0.2 wt.% Sn was found to promote the precipitation of θ′ and θ″ during heat treatments and stabilize the precipitates. The mechanism is also active in wrought Al-Mg-Si-Sn alloys [7].

However, the strengthening effect of Sn addition in Al-Si cast alloys was rarely observed. Kozana et al. [16] inferred additions of 0.2-1.7 wt.% Sn to an Al-10Si alloy caused the decrease in solidification points of α-Al according to their thermodynamic calculations, leading to drop in melt undercooling and microstructure refinement. As a result, the alloy's ultimate tensile strength was

 doi:10.20944/preprints202307.0963.v1

decreased. Qiu [17] et al. also found Sn addition led to the decrease in hardness of T6 treated A356 alloys by nearly 25%. The impairing effect of Sn was attributed by them to the generation of soft β-Sn phases, and the fact that the strengthening phase Mg2Si was replaced by Mg2Sn. However, the connection between cast defects and the deterioration effect of Sn on mechanical properties of Al-Si cast alloys was not studied. Therefore, this paper aims to clarify such a connection at multi-scales by 3D computed tomography, SEM and TEM.

2. Materials and Methods

The Al-9Si and Al-9Si-0.1Sn alloys were prepared, and the chemical compositions of these alloys are shown in Table 1. These two alloys were separately melted in argon in a CXZG-0.5 vacuum induction furnace from the raw materials including high purity (99.999 wt.%) Al particles, pure (99.99%) Mg particles, pure (99.9 %) Sn particles (Φ2 × 5 mm), master alloys Al-20Si, Al-10Fe, Al-10Mn and modifying alloys Al-10Sr (for refining Si particles), as well as grain refiner Al-5Ti-B (all in wt.% unless specified). The melt was poured into graphite mold to form rods of Φ20 mm × 10 mm.

Table 1. The alloys' chemical compositions (wt.%).

Si	Mg	Fe	Mn	Sr	Ti	Sn	Al
9	0.22-0.26	0.09-0.15	0.17-0.24	0.011-0.024	0.05-0.14	0 or 0.1	Bal.

The tensile samples (shown in Figure S1 in the Supplementary Document) wire-cut from the cast rods were tested on an Instron 3369 testing machine at room temperature and at a constant speed of 2 mm/min. 3 samples of the same state were tested to obtain a datapoint. The surfaces of fractured samples were ground, polished, and ultrasonically cleaned. The microstructures of the samples were observed by a Leica DM4500P optical microscope (OM) and a FEI Nova NanoSEM230 field emission gun scanning electron microscope (SEM) at 20 kV equipped with an energy dispersive spectrometer (EDS). The focused ion beam (FIB) machining was performed on a dual-beam scanning electron microscope (FEI Helios NanoLab G3 UC) employing a Ga liquid metal ion source, and electron backscattering diffraction (EBSD) experiments were also performed on such an instrument. The distribution of cast defects was studied by 3-dimention computed tomography (3DCT) on a Zeiss Xradia 620 Versa instrument, the sample size was 2×1×5 mm and resolution was 1.7 μm. The transmission electron microscopy (TEM) observations were performed on a Thermo Fisher Talos F200X field emission gun TEM operating at 200 kV. Interventionary studies involving animals or humans, and other studies that require ethical approval, must list the authority that provided approval and the corresponding ethical approval code.

3. Results and Discussion

3.1. Grain size

Sn can slightly refine the grain size of Al-Si alloys as shown in Figure 1. The brightest areas are α-Al phase. The eutectic Si phase is the grey contrast area. The black-contrast areas are pores or holes generated during casting. To avoid the interference of low Confidence Interval (CI) index signals, the EBSD data were cleaned up by OIM analysis software. Moreover, only the diameters of grains above 80 μm were counted to calculate the average diameters, which are 243.95 ± 125.53 μm and 203.15 ± 94.42 μm in the Sn-free and Sn-added samples, respectively. It is obvious that the grain size of the Al-9Si is slightly larger than the Al-9Si-0.1Sn. According to the Hall-Patch equation [18,19], this small difference of grain sizes leads to a very slight change of yield stress of about 0.43 MPa. Therefore, the strengthening effect due to refining of grain size by Sn addition is not obvious.

Preprints (www.preprints.org) | NOT PEER-REVIEWED | Posted: 14 July 2023 doi:10.20944/preprints202307.0963.v1

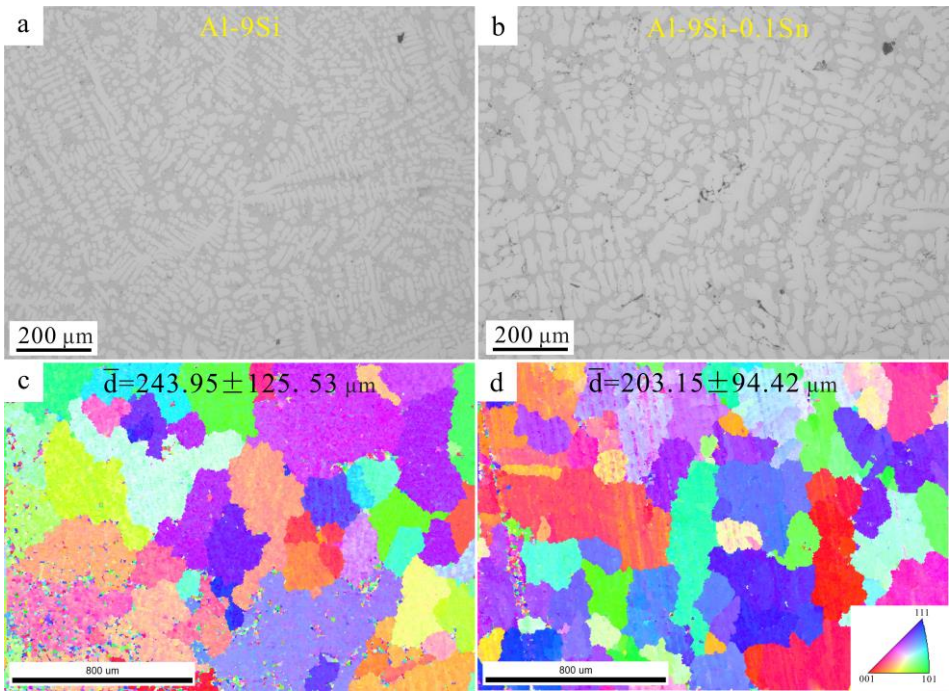

Figure 1. OM images (a and b) and IPFs (c and d) of Al-9Si alloys (a and c) and Al-9Si-0.1Sn alloys (b and d).

3.2. Pores and other cast defects caused by Sn

Most of Sn were found to be segregated near the oxide film, while others were oxidized during solidification, which caused the obvious cast defects and the increase in porosity. 3DCT visualization of the defects in the current cast alloys, as shown in Figure 2a,b and Supplementary Videos S1 and S2, reveals that the number of large pores is increased by about 90% due to the Sn addition. Furthermore, as shown in Figure 2c,d, the segregation of Sn can be found around the holes in the cast rods with Sn addition according to the EDS mapping results. Especially, some large cast cracks were found as shown in Figure 2d, and there are some white particles nearby. The corresponding EDS elemental maps show that the oxide layers (alumina bifilms [20]) lie on the cracks' edges, besides some large white particles comprised of O and Sn.

The precursors of oxide bifilms are the oxide film on the surface of the melt. Sn atoms seem to segregate near the oxide film [21], causing the decrease of local matrix solidification temperature [16]. When pouring the melting into the mold, the oxide films were rolled into the inner castings by turbulence [20]. Then, a quantity of liquid with high Sn solution was trapped in the enclosures which can't be refilled by others liquid. During solidification, some eutectic Si and Fe-containing phases were induced to nuclear on the bifilm in the early stage [20]. The possibility to generate enclosed areas increased. The solidification of the remaining Sn-rich liquid brings about shrinkage in the final state due to differences in thermal expansion coefficients (10.05×10^{-6} °C^{-1} for tin dioxide [22], 7.1×10^{-6} °C^{-1} for Alumina [23]). Some Sn combined with oxygen in matrix to generate tin oxide.

Preprints (www.preprints.org) | NOT PEER-REVIEWED | Posted: 14 July 2023 doi:10.20944/preprints202307.0963.v1

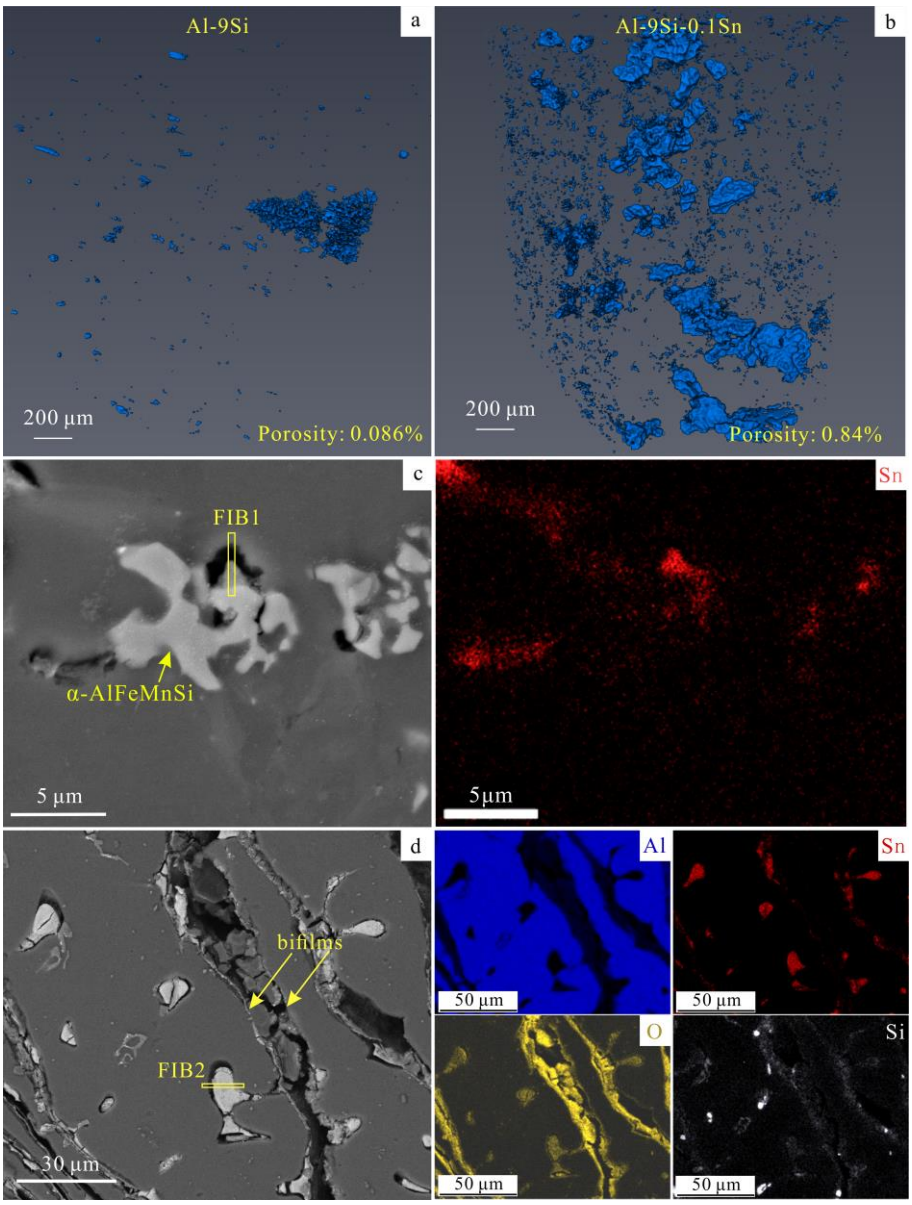

Figure 2. The morphology of cast defects. (a)The 3D cast defects of Al-9Si samples; (b) the 3D cast defects of Al-9Si-0.1Sn samples; (c) the SEM image of bifilm defects in the Al-9Si-0.1Sn sample maps; (d) the SEM image of hole defects in the Al-9Si-0.1Sn sample. EDS elemental maps are inserted in (c-d).

3.3. The structure and the composition of the Sn-containing particles

FIB1 and FIB2 areas marked in Figure 2c,d were extracted and thinned by FIB, and then observed by TEM. According to the high angle annular dark field (HADDF) images and corresponding EDS maps of FIB1, as shown in Figure 3c,e, Sn and Ca enrich in the area in yellow circle in Figure 3a. The select area electron diffraction (SAED) shows that this area consist of amorphous and polycrystals. However, the signals of polycrystals are too weak to index, probably some impurities containing oxides, nitrides, and calcium salts aggregated here.

The particles containing Sn and O are purely amorphous, according to the TEM results shown in Figure 3(f–j) from the FIB2 area. According to the high-resolution TEM (HRTEM) images and corresponding Fast Fourier Transform (FFT) patterns shown in Figure S2, after electron irradiation for seconds, the amorphous structure crystallized into SnO_2 (PDF #46-1088, P42/mnm), and the polycrystalline rings gradually appeared. Similar results have been reported in $Zr_{66.7}Cu_{33.3}$ alloys [24] and $Fe_{85}B_{15}$ alloys [25] by other researchers.

Preprints (www.preprints.org) | NOT PEER-REVIEWED | Posted: 14 July 2023 doi:10.20944/preprints202307.0963.v1

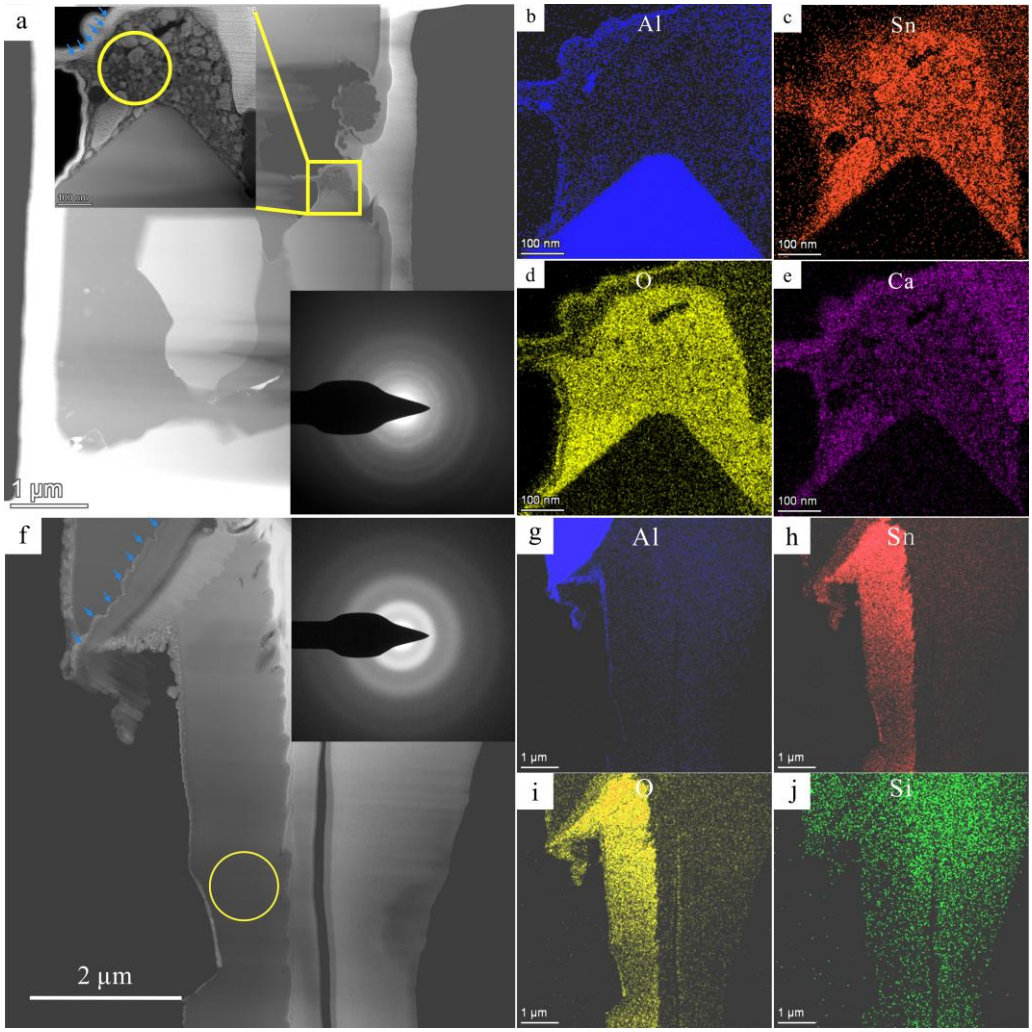

Figure 3. TEM results of FIB1 and FIB2 samples. (a) The HADDF-STEM image of FIB1 sample (Bottom inset is the SAED in yellow circle); (b-e) EDS maps of (a); (f) HADDF-STEM image of FIB2 sample (Inset is the SAED of yellow circle); (g-j) The EDS maps of (f). The blue arrows denote alumina films.

3.4. The mechanical behaviors of the cast defects

Tensile properties of Al-9Si and Al-9Si-0.1Sn samples are shown in Table 2. The stress-strain curves of all samples are shown in Figure S3. The results show that the ultimate tensile strength (UTS), yield strength (YS) and elongation (EL) are all diminished by adding Sn.

Table 2. The tensile properties of the alloys.

Sample	UTS/MPa	YS/MPa	EL/%
Al-9Si	269.92	144.26	8.24
Al-9Si-0.1Sn	213.55	113.47	6.62

The cast defects initiate cracks during tensile deformation, according to the SEM characterizations of fractured tensile samples shown in Figure 4. The EDS maps show the O and Sn are co-segregated in areas 1-5 marked in yellow circles in Figure 4a,g, which can be identified as tin oxides. These amorphous tin oxides are so brittle that they tend to break during tensile deformation (areas 1-5), in a manner similar to alumina [20].

Our work suggests not adding Sn in various cast Al alloys without heat treatments, as these fatal cast defects, including the pores and brittle amorphous tin oxides, do not depend on any third element.

Preprints (www.preprints.org) | NOT PEER-REVIEWED | Posted: 14 July 2023 doi:10.20944/preprints202307.0963.v1

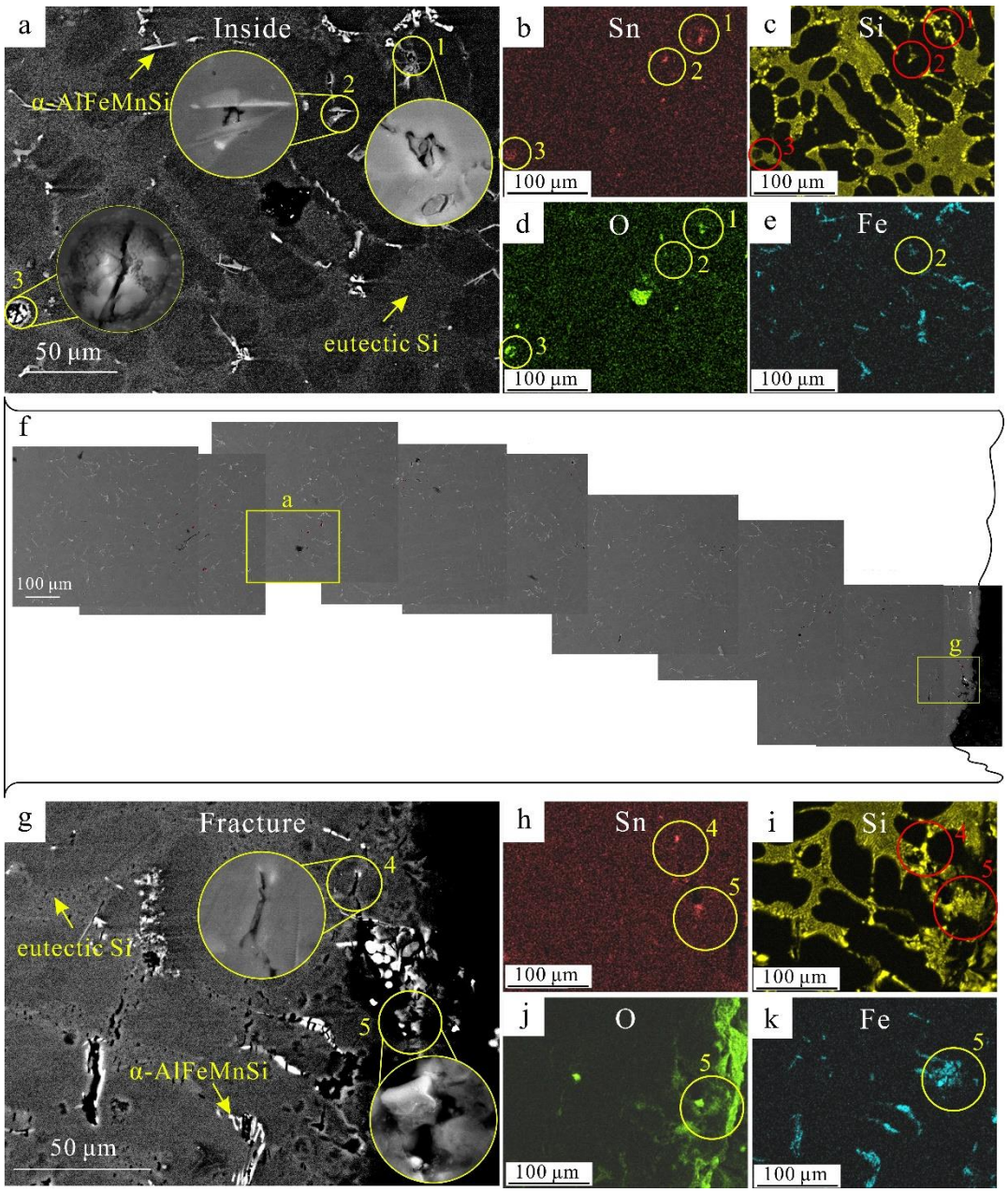

Figure 4. TEM results of FIB1 and FIB2 samples. (a) The HADDF-STEM image of FIB1 sample (Bottom inset is.

4. Conclusions

In this study, the fatal defects in cast Al-Si alloys due to Sn addition have been investigated by multi-scale characterizations.

(1) Sn can significantly deteriorate both strength and elongation, as it obviously increases the porosity, although meanwhile it slightly refines the grain size.

(2) During casting, melt with high Sn solution was trapped in the enclosures, shrinkage pores were then formed in cooling, and finally amorphous tin oxides were generated near the alumina films.

(3) These cast defects including the pores and brittle amorphous tin oxides, initiate cracks during tensile deformation.

(4) Our work suggests not adding Sn in various cast Al alloys without heat treatments, as these fatal cast defects do not depend on any third element.

Supplementary Materials: The following supporting information can be downloaded at the website of this paper posted on Preprints.org. Figure S1: The size of tension samples; Figure S2: The crystallization of amorphous. Figure S3: The stress-strain curves of Al-9Si and Al-9Si-0.1Sn samples. Figure S4: The enlarged details information of Figure 4f in text.; Video S1: The 3D reconstruction of 3DCT on Al-9Si sample; Video S2: The 3D reconstruction of 3DCT on Al-9Si-0.1Sn sample.

Author Contributions: conceptualization, Yao Xiao; methodology, Yao Xiao, Jicheng Wang, Qianyu Deng, Li Feng, Dianming Peng, Hui Feng and Kai Li; investigation, Yao Xiao, Jicheng Wang and Qianyu Deng; writing—original draft preparation, Yao Xiao; writing—review and editing, Yao Xiao, Jicheng Wang and Kai Li; formal analysis, Jicheng Wang, Dianming Peng and Hui Feng; funding acquisition, Yong Du and Kai Li.

Funding: This research was funded by National Natural Science Foundation of China, grant numbers 52071340 and 51820105001

Data Availability Statement: Data will be made available on request.

Acknowledgments: The authors thank the Advanced Research Center of CSU for assistance in TEM experiments.

Conflicts of Interest: The funders had no role in the design of the study; in the collection, analyses, or interpretation of data; in the writing of the manuscript; or in the decision to publish the results.

References

1. Kallas, M.K. Multi-directional unibody casting machine for a vehicle frame and associated methods. US20190217380A1, 18 July 2019.
2. Ye, H. An Overview of the Development of Al-Si-Alloy Based Material for Engine Applications. *J. Mater. Eng. Perform.* **2003**, *12*, 288-297.
3. Becker, H.; Bergh, T.; Vullum, P.E.; Leineweber, A.; Li, Y. Effect of Mn and cooling rates on α-, β-and δ-Al–Fe–Si intermetallic phase formation in a secondary Al–Si alloy. *Materialia* **2019**, *5*, 100198.
4. Roy, N.; Samuel, A.; Samuel, F. Porosity formation in Al-9wt% Si-3wt% Cu alloy systems: metallographic observation. *Metall. Mater. Trans. A* **1996**, *27*.
5. Zhang, L.; Gao, J.; Damoah, L.N.W.; Robertson, D.G. Removal of iron from aluminum: A review. *Miner. Process. Extr. Metall. Rev.* **2012**, *33*, 99-157.
6. Seifeddine, S.; Johansson, S.; Svensson, I.L. The influence of cooling rate and manganese content on the β-Al5FeSi phase formation and mechanical properties of Al–Si-based alloys. *Mater. Sci. Eng., A* **2008**, *490*, 385-390.
7. Lu, G.; Sun, B.; Wang, J.; Liu, Y.; Liu, C. High-temperature age-hardening behavior of Al–Mg–Si alloys with varying Sn contents. *J. Mater. Res. Technol.* **2021**, *14*, 2165-2173.
8. Banerjee, S.; Robi, P.; Srinivasan, A.; Lakavath, P.K. Effect of trace additions of Sn on microstructure and mechanical properties of Al–Cu–Mg alloys. *Mater. Des.* **2010**, *31*, 4007-4015.
9. Lotter, F.; Petschke, D.; De Geuser, F.; Elsayed, M.; Sextl, G.; Staab, T.E. In situ natural ageing of Al-Cu-(Mg) alloys: The effect of In and Sn on the very early stages of decomposition. *Scr. Mater.* **2019**, *168*, 104-107.
10. Lotter, F.; Petschke, D.; Staab, T.E.; Rohrmann, U.; Schubert, T.; Sextl, G.; Kieback, B. The influence of trace elements (In, Sn) on the hardening process of Al–Cu alloys. *physica status solidi (a)* **2018**, *215*, 1800038.
11. Liu, M.; Zhang, X.; Körner, B.; Elsayed, M.; Liang, Z.; Leyvraz, D.; Banhart, J. Effect of Sn and In on the natural ageing kinetics of Al–Mg–Si alloys. *Materialia* **2019**, *6*, 100261.
12. Lin, Q.; Zhong, W.; Li, F.; Yu, W. Reactive wetting of tin/steel and tin/aluminum at 350–450° C. *J. Alloys Compd.* **2017**, *716*, 73-80.
13. Akopyan, T.K.; Belov, N.A.; Letyagin, N.V. Effect of trace addition of Sn on the precipitation hardening in Al-Si-Cu eutectic alloy. *JOM* **2019**, *71*, 1768-1775.
14. Elsayed, M.; Staab, T.E.; Čížek, J.; Krause-Rehberg, R. On the interaction of solute atoms with vacancies in diluted Al-alloys: A paradigmatic experimental and ab-initio study on indium and tin. *Acta Mater.* **2021**, *219*, 117228.
15. Elsayed, M.; Staab, T.E.M.; Čížek, J.; Krause-Rehberg, R. On the interaction of solute atoms with vacancies in diluted Al-alloys: A paradigmatic experimental and ab-initio study on indium and tin. *Acta Mater.* **2021**, *219*, 117228, doi:https://doi.org/10.1016/j.actamat.2021.117228.

16. Kozana, J.; Piękoś, M.; Garbacz-Klempka, A.; Perek-Nowak, M. The Effect of Tin on Microstructure and Properties of the Al-10 wt.% Si Alloy. *Materials* **2022**, *15*, 6350.
17. Ke, Q.; Wang, R.-C.; Peng, C.-q.; Wang, N.-G.; Cai, Z.-y.; Zhang, C. Effect of individual and combined additions of Al–5Ti–B, Mn and Sn on sliding wear behavior of A356 alloy. *Trans. Nonferrous Met. Soc. China* **2015**, *25*, 3886-3892.
18. Hall, E. The deformation and ageing of mild steel: III discussion of results. *Proceedings of the Physical Society. Section B* **1951**, *64*, 747.
19. Petch, N. The cleavage strength of polycrystals. *Journal of the iron and steel institute* **1953**, *174*, 25-28.
20. Gopalan, R.; Prabhu, N.K. Oxide bifilms in aluminium alloy castings–a review. *Mater. Sci. Technol.* **2011**, *27*, 1757-1769.
21. Kondoh, K.; Kimura, A.; Watanabe, R. Analysis of tin behaviour on surface of rapidly solidified aluminium alloy powder particles during heating. *Powder Metall.* **2001**, *44*, 253-258, doi:10.1179/003258901666428.
22. Wang, B.; Yang, Y.; Yang, G. Electron-beam irradiation induced shape transformation of Sn–SnO2 nanocables. *Nanotechnology* **2006**, *17*, 5916.
23. Bernard, M.; Pateloup, V.; Passerieux, D.; Cros, D.; Madrangeas, V.; Chartier, T. Feasibility of manufacturing of Al2O3–Mo HTCC by hybrid additive process. *Ceram. Int.* **2022**, *48*, 14993-15005.
24. Nagase, T.; Umakoshi, Y. Phase stability of amorphous and crystalline phases in melt-spun Zr66. 7Cu33. 3 alloy under electron irradiation. *Scr. Mater.* **2003**, *48*, 1237-1242.
25. Qin, W.; Nagase, T.; Umakoshi, Y. Electron irradiation-induced nanocrystallization of amorphous Fe85B15 alloy: Evidence for athermal nature. *Acta Mater.* **2009**, *57*, 1300-1307.